

Densification and Distortion in Selective Laser Sintering of Polycarbonate

M. Berzins, T. H. C. Childs, K. W. Dalgarno, G. R. Ryder and G. Stein,

University of Leeds, LS2 9JT, UK

The creation of a 3D numerical model for real part accuracy simulations is the goal of this work. An improvement of a first attempt to predict densification, which used a classical moving heat source calculation and a viscous sintering model, is reported: it includes a numerical thermal calculation with thermal properties allowed to vary with temperature. A study of polycarbonate part 'curl' distortion is also reported. The development of curl at part edges and with part thickness is followed. Mechanical and thermal reasons are sought as to why the distortion is concentrated at edges.

INTRODUCTION

Geometry errors in a selective laser sintered part have two processing causes. The sintering process allows the sintered envelope to differ from the envelope traversed by the centre of the laser beam; the offset between the envelopes causes linear errors to the extent that the offset is not controlled. Thermal distortions give rise to both linear (shrinkage) and geometric (warping) errors: for polymer parts warping can occur both during building at elevated temperature and later on cooling to room temperature. This paper is about modelling the sintering process and about warping.

A previous study of the sintering of polycarbonate parts by a scanning laser beam analysed the creation of thin rectangular plates lying horizontally in the powder bed and with edges parallel and perpendicular to the laser raster direction (1). Modelling proceeded by replacing the scanning laser spot by an equivalent blade of laser heat and using classical moving heat source theory (1,2) to calculate the temperature / time history of powder in and round the edges of the part envelope. When combined with a viscous powder sintering model (1,3), predictions of part density and size were made. Both density and size errors depended on the laser heat flux (J/mm^2) into the surface, given by $P/(Us)$ where P is the laser power, U is the scan speed and s the separation between laser rasters (this has also been found by others (4)). Good agreement with experiment was found when the room temperature conductivity and specific heat of solid polycarbonate were used in the temperature calculation. This is surprising as the polycarbonate was not solid or at room temperature. This paper reports developments of this work, aimed at establishing what are the key physical properties that must be included in a sintering model eventually to be a practical 3D prediction tool.

As for warping, differential thermal contraction can cause uniform curvature of flat plates to develop during post-process cooling of polymer sintered parts to room temperature (5). Another type of curvature develops during the manufacture of flat plates lying horizontally in the powder bed. It is concentrated at the lower edges of the plates and called curl. It does not seem to have been asked why this curvature is confined to edges, nor is it obvious. It has visual similarities with the spalling of thin films from

substrates (6,7) and this may imply that failure of cohesion between a plate and supporting powder is relevant to curl development. However, spalling differs from curl in that it is not constrained to thin film edges; it is catastrophic: spalling cracks run almost right through an interface. Experimental studies of curling and theory for residual strain and stress development is reported, to try to explain why, in selective laser sintering, the large curvatures that can occur on downward facing nominally flat surfaces are confined to edges.

THEORY

Sintering. Densification depends on temperature and time; temperature depends on conductivity k , specific heat C_p and density; k in turn depends on densification. The flow chart of a computer programme that develops by iteration a consistency between an assumed and calculated sintered density is shown in figure 1. It also allows for radiation heat loss by adjusting this until the heat from the laser equals that flowing into the part plus that lost by radiation. The temperature calculation, part of the sintered density calculation, can either be the analytical method (1) or a finite difference calculation: a public domain adaptive mesh finite difference package expected to be supported as part of the NAG library has been used (8). A linear 2D version has been implemented, but it has capacity for extension to a non-linear 3D form. Thermal properties varying with temperature ($^{\circ}\text{K}$) are included (C_p in J/kg and k in $\text{W/m}^{\circ}\text{K}$, simplified from ref. 3):

$$C_p = 935 + 2.28T \quad k_{\text{solid}} = 0.0251 + 0.0005T \quad k_{\text{sinter}} = k_{\text{solid}} (\rho / \rho_{\text{solid}}) \quad (1)$$

Curl development. The interfacial stresses set up between a thin layer of Young's modulus E and a rigid substrate, due to a thermal contraction strain ϵ in the thin layer, have been studied by an elastic finite element (fe) calculation. Two cases have been considered (figure 2): the layer bonded totally to the substrate; and a layer already separated at one end. A cooling melt layer (as in selective laser sintering) is not elastic but visco-elastic. A conceptual model of such a melt layer bonded to an elastic foundation (shown as part of figure 14) has been analysed to determine the evolution of strain with time. It can be shown that the compressive strain ϵ_f in the foundation at time t when the melt has experienced a temperature drop of ΔT since time $t = 0$ is given by

$$\dot{\epsilon}_f \left(1 + \frac{E_f}{E_m} \right) + \epsilon_f \left(\frac{E_f}{\eta} + \frac{E_{m2}}{\eta} + \frac{E_{m2} E_f}{\eta E_{m1}} \right) = - \frac{E_{m2} \alpha \Delta T}{\eta} - \alpha \frac{dT}{dt} \quad (2)$$

where α is the thermal contraction coefficient of the film, and the moduli are defined in figure 14a. Equation 2 can be solved as an initial value problem, with $\epsilon_f = 0$ at $t = 0$. The fe and strain estimates are used to gain insight into the conditions of curling.

EXPERIMENTATION

Sintered density experiments. Data reported previously (1) on the dependence of density on $P/(Us)$ has been used to assess the modelling developments.

Curl development experiments. Rectangular plates 90 mm x 26 mm in area and 1, 2, 3, 5, 10, 20 and 50 layers thick have been sintered in a Sinterstation 2000 machine. The plate thicknesses and the profiles of their bottom surfaces have subsequently been measured with a micrometer and stylus profilometer. The nominal layer thickness was 0.125 mm, $P = 10$ W, $U = 1,189$ mm/s and $s = 0.15$ mm. The powder bed was at 154°C. No base was used in these tests: a base is a raft of lightly sintered powder built immediately below a part to anchor its first few layers during building. In further tests, 50 layer thick parts were built to study the effect of bases on curl. Bases were built with $P = 10$ W, $U = 1,189$ mm/s but with a range of scan spacings from 0.15 to 0.63 mm.

EXPERIMENTAL AND THEORETICAL RESULTS

Sintered densities. Figure 3 records how sintered densities varied experimentally (●) with laser flux. Figure 3a compares these with predictions from the analytical modelling. The upper and lower dashed lines labelled P (for powder) and S (for solid) are predictions without the iterative density loop of figure 1. P results when room temperature powder thermal properties are used in the temperature calculation and S when properties of the solid are used. The solid lines all refer to the use of the iterative development: (i), (ii) and (iii) result when thermal properties for 300°K, 600°K and 800°K are used respectively. (iii) is a good fit with experiment but there is no independent basis for this choice of thermal properties. Figure 3b contains the predictions from 2D finite difference thermal modelling. Curve (i) has constant thermal properties appropriate to 600°K : its agreement with curve (ii) in figure 3a is a check on the numerical method's accuracy. Curve (ii) has thermal properties varying according to equations 1: it closely predicts densities, but slightly overestimates them at low energy fluxes and underestimates them at high fluxes. In all the calculations the inclusion of radiant heat loss had no significant effect on temperature: it can be neglected from sintering considerations for polymers.

Curl development. Figure 5 traces the edge profiles of parts 1 to 50 layers thick, where the part co-ordinate system is defined in figure 4. The 1 layer part has a downward curl but this is an artefact caused by placing a thin (very flexible) upward curling part upside down on a flat plate in order to measure its profile. Figure 6 shows how the derived slopes vary with distance from the edge. Linear slope variation with x indicates a circular profile: all the profiles can be approximated to 2 circular arcs. The 50 layer thick parts showed a uniform curvature far from their edges. Figure 7 shows a measured slope variation with x over the range $x > 15$ mm. The much lower change of slope with x indicates a much larger radius (≈ 6 m) than for $x < 15$ mm.

In figure 6, a region I of steep slope is seen close to the edge ($x < 2.5$ mm) and a region II of lesser slope for $2.5 < x$, mm < 12.5 . The region II spreads further the thicker is the part. The radius as a function of x has been estimated from $1/(d^2y/dx^2)$ and is plotted in figure 8. The 2 layer thick part has an edge curled to a radius of 10 mm over a length of 2.5 mm and a further curl developed over $x = 2.5$ to 4 mm, with a radius increasing to 15 mm. (The 1 layer thick part was found to have only the 2.5 mm length of 10 mm radius.) As extra layers are added, the pre-existing curl is not much changed, but the length of curled region grows and the radius increases, until for $x > 5$ mm the

radius becomes constant at 55 to 60 mm. Once parts are between 20 and 50 layers thick, and the length of curled region has become 12.5 mm, no further curl occurs. The length e of curled region, considered as having parts e_I and e_{II} corresponding to regions I and II in figure 6, is further considered in figure 9. The length e_{II} stops growing when the part thickness, h , reaches 4 mm; by then, the initial value of e_{II}/h of 5 has dropped to 3.

The influence of a base on curl profile is shown in figures 10 and 11. Neither the initial radius R_I nor the length e of curled edge is changed by a base (figure 10) but R_{II} depends on the laser flux used to build the base (figure 11). Figure 11 shows the base has no restraining effect on curl until a flux greater than 0.015 J/mm^2 is used. Increasing the flux to 0.03 J/mm^2 fully develops the restraint: this flux causes densification in the base to a level of 560 kg/m^3 (figure 3).

Causes of curling have been searched for. The edge shape of a single layer part has been estimated from analytical calculations of the temperature / time histories of points near the surface of a powder bed, round the edge of a rectangular envelope scanned by a laser beam. Sintered density contours derived from these histories are shown in figure 12. Curved contours are seen which correspond to a corner of radius of 0.5 to 1 mm, one tenth the value of the initial curl radius of region I. (Microscopic observation does indeed show such a fine edge radius to exist, but it has no relevance to curl.) Finite element calculations (figure 2) show tensile interfacial stresses to exist for $x/h < 0.5$ and shear stresses to exist for $x/h < 3$ (figure 13). They are the same for both the uncracked and cracked interface cases. These x/h values are less than the observed e/h extents. Further, if the stresses are responsible for the curl, the model gives no reason why the curl should be limited to the part edges. Finally figure 14 summarises the viscoelastic residual strain calculations from equation 2. Significant strains only develop once the melt temperature drops to $< 190^\circ\text{C}$. In this rubbery region, the modulus E_{m1} (figure 14a) was supposed infinite, to create a Voigt model. The melt modulus and viscosity were assumed to vary with temperature as in figure 14b (the viscosity values are extrapolated to lower temperatures from capillary rheometer data in (3), using a WLF transform (9)), and E_f was taken to be 10^8 Pa (the foundation is at 154°C). Figure 14c shows a build up of residual strain to reach value from $- (3.3 \text{ to } 6.4) \times 10^{-3}$ at 155°C , depending on cooling rate from 0.1 to $10 \text{ }^\circ\text{C/s}$.

The density contours in figure 12 have no allowance made for the shrinkage that the densification implies. The vertical marker indicates a derived shrunk layer thickness of 0.33 mm. The measured thickness of a single layer was 0.61 mm.

DISCUSSION AND CONCLUSION

The thermal sintering calculations have demonstrated that variation of thermal properties with temperature must be taken into account in modelling, but radiation can be ignored. An attempt to predict the thickness of a single layer part (figure 12) underestimates thickness by a factor of 2. At the time of preparing this paper it was being studied numerically whether allowance for densification on thermal properties, concurrently within the temperature calculation, would remove this discrepancy and thus add a further essential factor to be included, as suggested in (4).

Part curvature exists on several scales. Sintering calculations (figure 12) have given radii from 0.5 to 1 mm for an edge extent $e < 0.5 \text{ mm}$ at the edges of single layers. At the other

extreme a general warpage radius of 6 m has been measured (figure 7). In between, a curl radius of 10 mm, not affected by bases, has been measured for e up to 2.5 mm on single layers. As multiple layers are built, curl extends until e reaches 12.5 mm for a part 4 mm thick; thereafter no further curl develops (figures 8,9). The radius of curl more than 5mm from an edge is affected by bases, varying from 60 mm with no base to 200 mm (figure 11). We speculate that the two levels of curl have different causes: the 10 mm radius is due to sintering shrinkage while the 60 to 200 mm radii arise from thermal contraction as a melt layer cools back to 154°C. In the latter case, the elastic calculation (figure 13) gives no reason why curl is confined to edges. There must be a cohesion with supporting powder to prevent the spread of curl. The calculations of figure 13 and the viscoelastic strain estimates of figure 14 suggests a cohesion strength in the range 0.1 to 1 MPa. Figure 14 shows the strain reduces with reducing cooling rate. Perhaps curl is confined to edges because a larger cooling rate at edges causes larger stresses there. A full explanation of this, with better viscoelastic modelling, awaits further work.

ACKNOWLEDGEMENT

One of us (GRR) wishes to thank the Keyworth Institute of the University of Leeds for a research scholarship.

REFERENCES

1. Childs T. H. C., Cardie S. and Browne J. M., Selective laser sintering of polycarbonate at varying powers, scan speeds and spacings, Proc. Solid Free Form Fabrication Symposium 1994, pp 356-363, The University of Texas at Austin 1994.
2. Jaeger J. C., Moving sources of heat and the temperature at sliding contacts, Jnl. Roy. Soc. New South Wales, 1942, 76, 203-224.
3. Nelson J. C. et al., Model of the selective laser sintering of bisphenol-A polycarbonate, Ind. Eng. Chem. Res., 1993, 32, 2305-2317.
4. Nelson J. C., Selective laser sintering: a definition of the process and an empirical sintering model, PhD thesis, The University of Austin at Texas, 1993.
5. Amon C. et al., Material issues in layered forming, Proc. Solid Free Form Fabrication Symposium 1993, pp 1-10, The University of Texas at Austin 1993.
6. Thouless M. D., Evans A. G., Ashby M. F. and Hutchinson J. W., Tee edge cracking and spalling of brittle plates, Acta Metall., 1987, 35, 1333-1341.
7. Drory M. D., Thouless M. D. and Evans A. G., On the decohesion of residually stressed thin films, Acta Metall., 1988, 36, 2019-2028.
8. Blom J. G. and Verwer J. G., VLUGR2: a vectorised local uniform grid refinement code for PDEs in 2D, report NM-R9306, CWI, Amsterdam 1993.
9. Tadmor Z. and Gogos C. G., Principles of Polymer Processing, Ch. 9.2, Wiley New York, 1979.

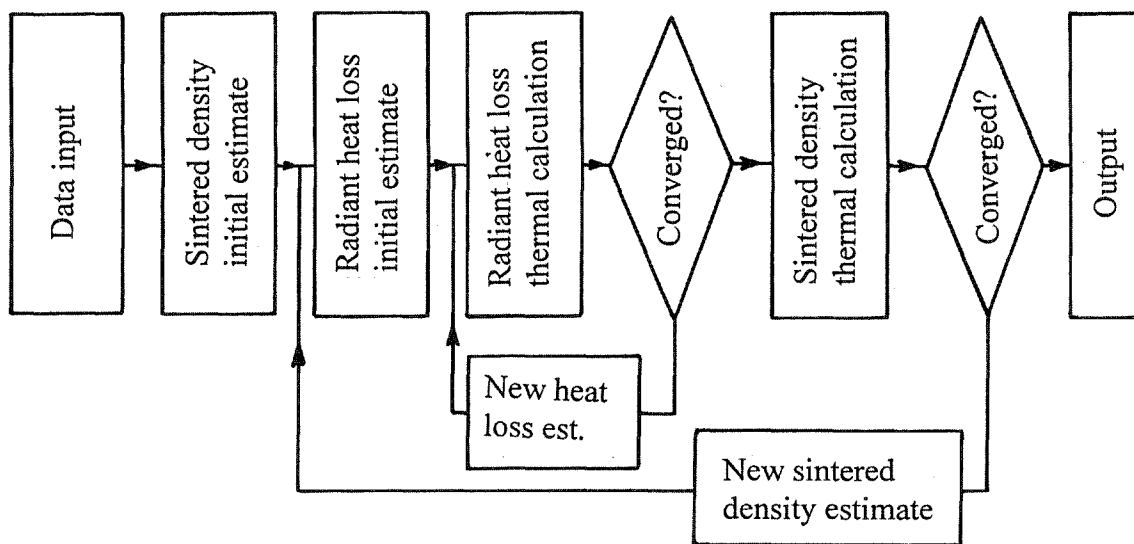


Figure 1. Thermal calculation flow chart.

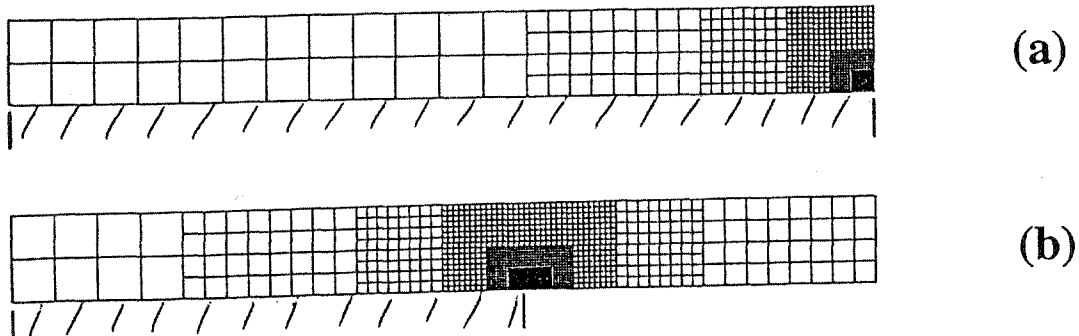


Figure 2. Finite element meshes for a thin elastic layer adhered to a rigid substrate, (a) over all its length, (b) with a crack at one end.

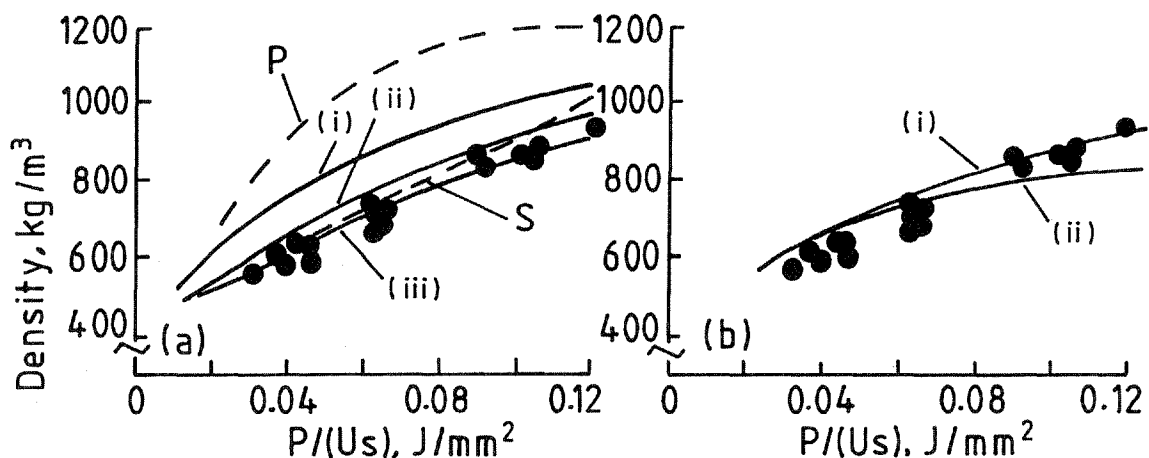


Figure 3. (a) analytical and (b) numerical sintered density estimates, as described in text; • = experimental results.

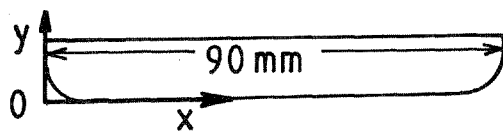


Figure 4. Schematic part section, to define x-y axes.

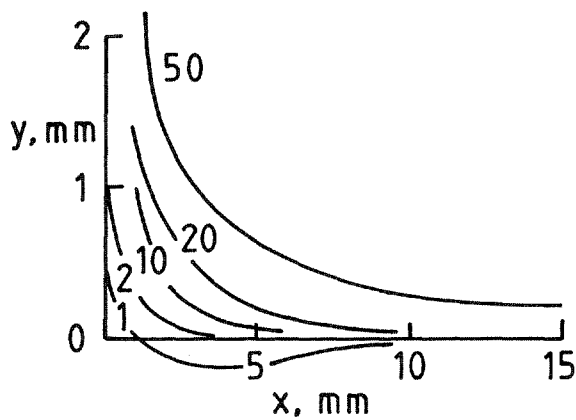


Figure 5. Measured profiles of 1, 2, 10, 20 and 50 layer parts.

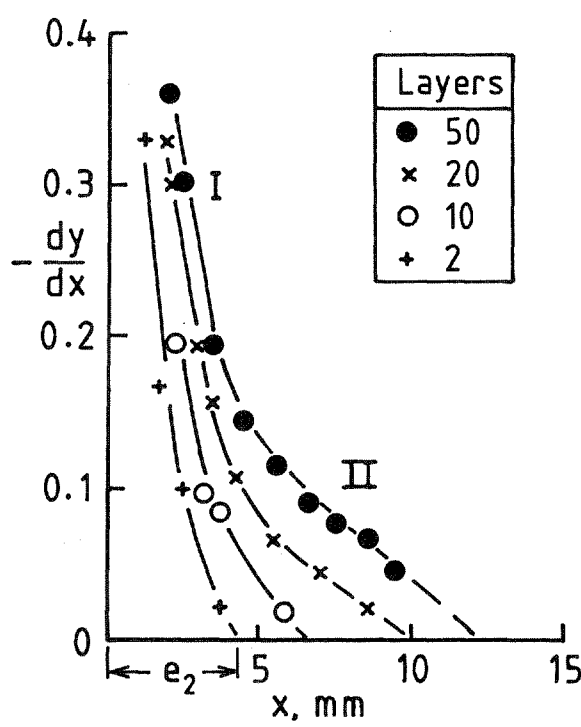


Figure 6. Slope variations of parts 2, 10, 20 and 50 layers thick.

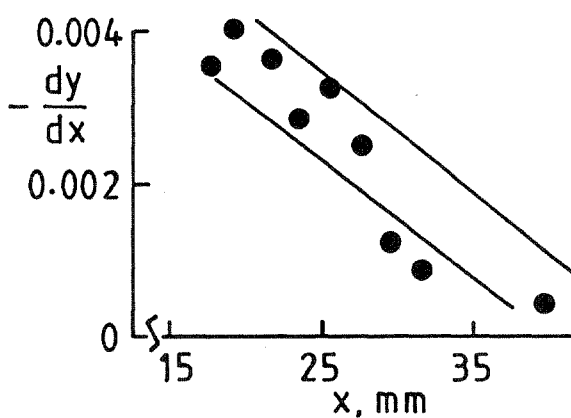


Figure 7. Slope variations far from edge, 50 layer thick part.

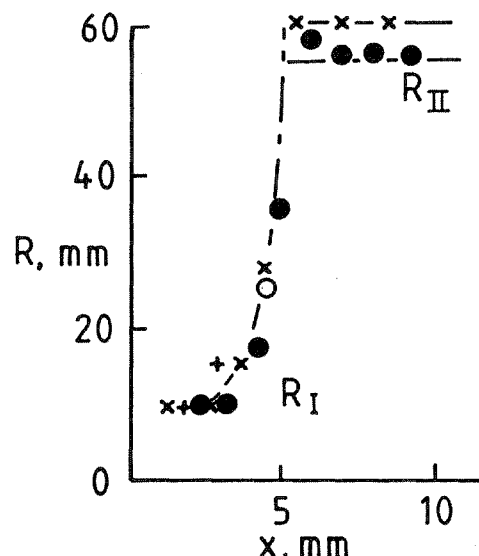


Figure 8. Variations of R with x, symbols as figure 6.

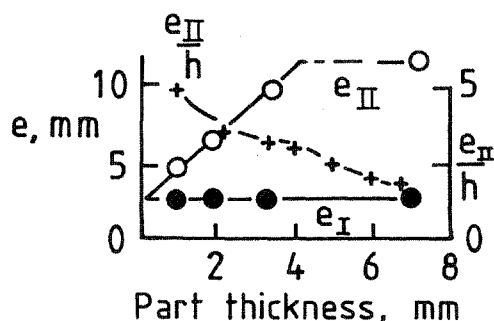


Figure 9. Variations of e with part thickness.

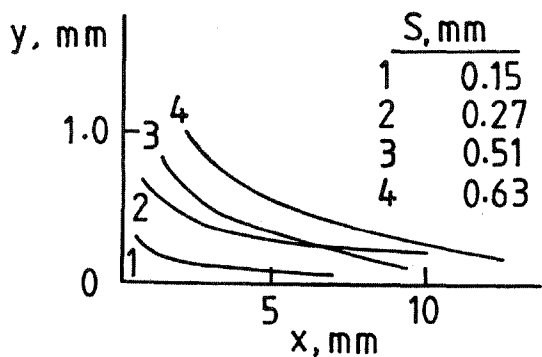


Figure 10. Profiles of 50 layer parts made with a range of bases.

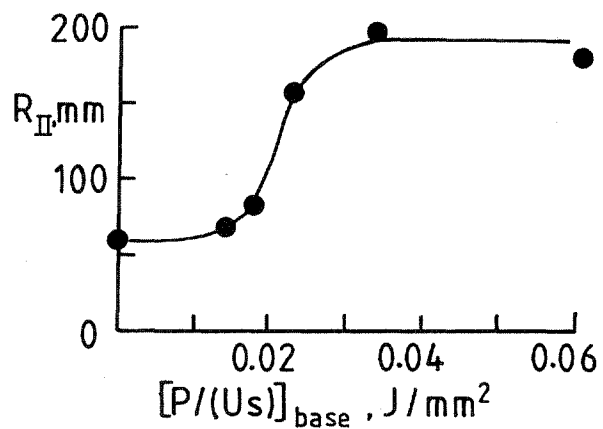


Figure 11. R_{II} values as a function of base condition.

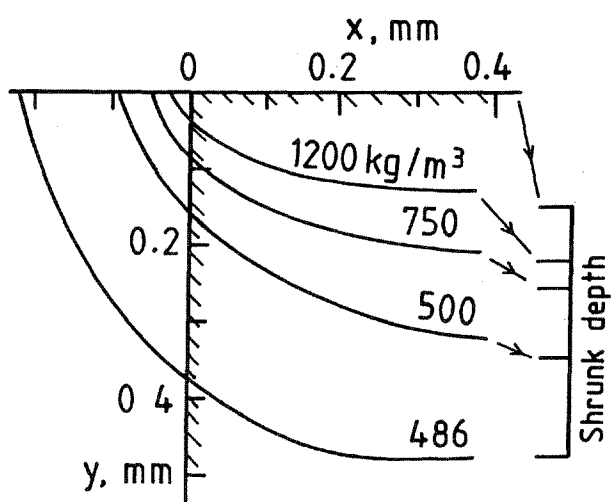


Figure 12. Estimated density contours at a single layer edge, and derived shrinkage; $P/(Us) = 0.062 \text{ J/mm}^2$.

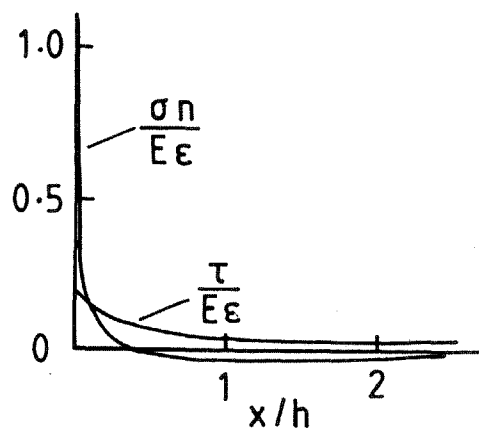


Figure 13. Interfacial stress variation with distance from edge.

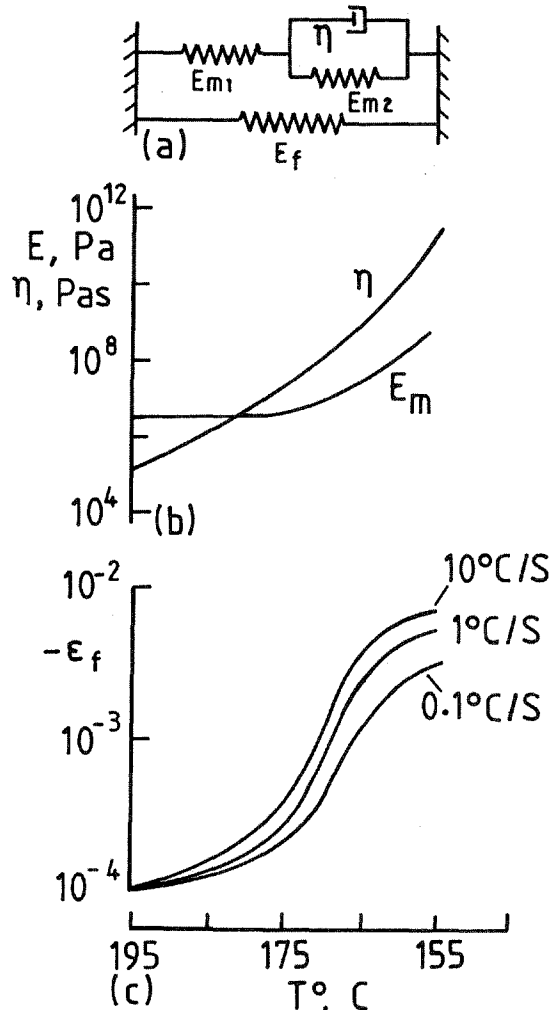


Figure 14. (a) viscoelastic model, (b) values of E and η and (c) resulting strain development with cooling.